

# Hydro-morphodynamics 2D modelling using a discontinuous Galerkin discretisation

Mariana C. A. Clare<sup>a,\*</sup>, James R. Percival<sup>a</sup>, Athanasios Angeloudis<sup>b</sup>, Colin J. Cotter<sup>c</sup> and Matthew D. Piggott<sup>a</sup>

<sup>a</sup>Department of Earth Science and Engineering, Imperial College London, UK.

<sup>b</sup>School of Engineering, Institute for Infrastructure & Environment, University of Edinburgh, UK.

<sup>c</sup>Department of Mathematics, Imperial College London, UK.

---


## 1. Introduction

Data from 2010 shows that almost 400 million people lived in areas less than 5m above average sea level (CIESIN, 2013) and this population keeps growing. As sea levels rise and with the potential for storms to increase in strength and frequency due to a changing climate, the coastal zone is becoming an ever more critical location for the application of advanced modelling techniques. A particularly important example is the development and application of improved morphodynamic models to simulate sediment transport accurately. The effects of climate change will cause hydrodynamic changes leading to increased erosion rates, increasing flooding and erosion risk in coastal zones. The coupled and non-linear nature of this problem makes it especially challenging, since models must solve both hydrodynamic and sediment transport processes together with their two-way coupled interactions. Furthermore, there are two types of sediment transport processes that should be resolved: suspended sediment in the fluid and bedload transport propagating along the bed itself.

Over the last 40 years, increasingly complex morphodynamic models have been developed to predict sediment transport in fluvial and coastal zones. These models can be one-dimensional (1D), two-dimensional (2D) or three-dimensional (3D), and are discussed in detail in Amoudry (2008), Amoudry and Souza (2011) and Papanicolaou et al. (2008), which we draw upon for a brief review here. 1D models generally use finite difference methods to solve a simple system of equations and are the cheapest computationally. However, they cannot capture velocity in the cross-stream and vertical directions. 2D (or 2DH) models adopt the shallow water approximation and can use finite difference (e.g. XBeach – Roelvink et al., 2015), finite volume (e.g. Mike 21 – Warren and Bach, 1992), or finite element based methods to solve a more complex system of equations. They capture velocity in both the streamwise and cross-stream directions on planview geometries in the horizontal. 3D models are similar to 2D, but solve an even more complex full system of equations using finite difference (e.g. ROMS – Warner et al., 2008), finite volume (e.g. Fast3d – Landsberg et al., 1998) or finite element based methods. They are thus potentially more accurate, but considerably more computationally expensive. More sophisticated models offer 2D and 3D options, such as Telemac-Mascaret (Hervouet, 1999) and Delft3d (Deltares, 2014), which use finite element/volume and finite difference based methods, respectively. In choosing a model, one must balance the simplicity and computational efficiency of a 2D model against the potential accuracy of a 3D one.

Despite this variety of approaches, Syvitski et al. (2010) argue the need for more accurate and faster morphodynamic models. The aim of this work is to present a novel and flexible 2D depth-averaged coupled hydrodynamic and sediment transport model developed within *Thetis*, a finite element coastal ocean modelling system (Kärnä et al., 2018) built using the *Firedrake* code generation framework (Rathgeber et al., 2017). This framework is versatile and ensures our underlying code is robust and optimised, and can be executed efficiently in parallel. Furthermore, it means our model is easily extensible and further work could include using an adjoint allowing a sensitivity analysis to be conducted (Farrell et al., 2013) or using an adaptive mesh resulting in a decrease in computational cost (McManus et al.,

---

 [m.clare17@imperial.ac.uk](mailto:m.clare17@imperial.ac.uk) (M.C.A. Clare)

---

### Author credits

**Mariana C. A. Clare:** Code development and verification, experimental design, manuscript preparation. **James R. Percival:** Technical supervision, manuscript review and editing. **Athanasios Angeloudis:** Technical supervision, manuscript review and editing. **Colin J. Cotter:** Project supervision, manuscript review and editing. **Matthew D. Piggott:** Project supervision, manuscript review and editing.

2017).

In this work, a 2D model is an appropriate choice because the depth-scale is much smaller than the horizontal for the cases discussed. We extend *Thetis*' existing capability to model scalar transport to a capacity to model suspended sediment transport and add within it a new capability to model bedload transport and bedlevel changes. For validation purposes, we compare our results with experimental data and Telemac-Mascaret's 2D model (Hervouet, 1999), which is widely-used (Amoudry and Souza, 2011; Papanicolaou et al., 2008). We improve on existing state-of-the-art models by using a discontinuous Galerkin based finite element discretisation (DG) available in *Thetis* (Kärnä et al., 2018). DG has several advantages including being locally mass conservative, meaning sediment is conserved on an element-by-element level, which is an advantage for coupling (Dawson, Sun and Wheeler, 2004); being well-suited to advection-dominated problems like ours (Kärnä et al., 2018); being geometrically flexible; and allowing higher order local approximations (Li, 2006). Morphodynamic models using DG have been presented in Kubatko, Westerink and Dawson (2006), Michoski et al. (2013) and Tassi et al. (2008), but without suspended sediment transport. To the best of our knowledge, our model is the first morphodynamic model with both bedload and suspended sediment transport to use DG.

The remainder of this paper is structured as follows: in Section 2 we describe our coupled hydrodynamic and sediment transport model; in Section 3 we explore the finite element model *Thetis*; in Sections 4 and 5, we use the test cases of a migrating trench and a meander to validate our model; in Section 6 we benchmark our test cases against *Sisyphé* and finally in Section 7 conclude this work.

## 2. Model derivation

### 2.1. Hydrodynamic and sediment transport equations

In this subsection, we describe the general equations for modelling the hydrodynamic and sediment transport flow, and follow the presentation and notation of Wu (2007), where more details can be found.

The hydrodynamic component of the sediment-water mixture is governed by the (3D) Navier-Stokes equations for single phase flow. We use the 2D version of *Thetis* assuming the only external force acting on the system is gravity. We also assume any wavelength is much longer than the depth of the fluid, hence the vertical flow variation is small enough to be negligible and  $\partial u_1/\partial z = \partial u_2/\partial z = 0$  (for more details, see Segur, 2009).

The 2D model is derived by depth-averaging from the bed,  $z_b$ , to the water surface,  $\eta$ , the hydrodynamic equations. Thus, we must define conditions at the fluid boundaries: we apply the kinematic boundary condition at  $\eta$  as a free moving boundary, and we consider  $z_b$  to be impermeable. Since the bed evolution is slow, imposing a no-slip condition at  $z_b$  means  $u_1 = u_2 = 0$  here and thus the simplified depth-averaged equation for the conservation of mass is

$$\frac{\partial \eta}{\partial t} + \frac{\partial}{\partial x}(h\bar{u}_1) + \frac{\partial}{\partial y}(h\bar{u}_2) = 0, \quad (1)$$

where  $h = \eta - z_b$  is the depth, and  $\bar{u}_1$  and  $\bar{u}_2$  are the depth-averaged velocities in the  $x$  and  $y$  directions, respectively. Note that following convention, depth-averaged variables are denoted with an overbar, as  $\bar{\cdot}$ .

Applying the boundary conditions, combining dispersion and stress effects, and assuming there is no wind-driving force on the water surface, the simplified depth-averaged equation for the conservation of momentum is

$$\frac{\partial(h\bar{u}_i)}{\partial t} + \frac{\partial(h\bar{u}_1\bar{u}_i)}{\partial x} + \frac{\partial(h\bar{u}_2\bar{u}_i)}{\partial y} = -gh\frac{\partial \eta}{\partial x_i} + \frac{1}{\rho}\frac{\partial(h\bar{\tau}_{i1})}{\partial x} + \frac{1}{\rho}\frac{\partial(h\bar{\tau}_{i2})}{\partial y} - \frac{\tau_{bi}}{\rho}, \quad (2)$$

where, following the notation of Wu (2007),  $\bar{\tau}_{ij} = \mu_t \left( \frac{\partial \bar{u}_i}{\partial x_j} + \frac{\partial \bar{u}_j}{\partial x_i} \right)$  and  $\mu_t$  is the dynamic eddy viscosity. Note that  $i = 1, 2$  represents the  $x, y$ -direction. Eq. (1) and (2) comprise the hydrodynamic component of our model.

We take an Eulerian approach for the sediment transport equations, rather than the more computationally expensive Lagrangian approach, and make a macroscopic assumption. We thus represent the sediment dynamics via an advection-diffusion equation for a sediment concentration field,  $c$ . Note that in this work we only consider non-cohesive sediment.

If the sediment diameter is finer than 1 mm and the sediment concentration,  $c$ , is lower than 10% of the fluid volume then we can assume there is no mixing at the 'molecular level'. Hence, there is no diffusion and the only significant relative motion between the flow and the sediment is settling due to gravity. Furthermore, the low concentration and

fine sediment size means the settling velocity of the sediment particles  $w_s$  can be approximated by that of a single sediment particle in clear water. The equation governing the sediment concentration is

$$\frac{\partial c}{\partial t} + \frac{\partial(u_j c)}{\partial x_j} = \frac{\partial}{\partial x_j} (w_s c \delta_{3j}), \quad (3)$$

where  $\delta_{3j}$  is the Kronecker delta applied to the vertical component. Time-averaging Eq. (3) to filter turbulence introduces a diffusivity term,  $\epsilon_s \frac{\partial c}{\partial x_j}$ , and becomes

$$\frac{\partial c}{\partial t} + \frac{\partial(u_1 c)}{\partial x} + \frac{\partial(u_2 c)}{\partial y} + \frac{\partial(u_3 c)}{\partial z} - \frac{\partial(w_s c)}{\partial z} = \frac{\partial}{\partial x} \left( \epsilon_s \frac{\partial c}{\partial x} \right) + \frac{\partial}{\partial y} \left( \epsilon_s \frac{\partial c}{\partial y} \right) + \frac{\partial}{\partial z} \left( \epsilon_s \frac{\partial c}{\partial z} \right), \quad (4)$$

67 where  $\epsilon_s$  is the so-called sediment turbulent diffusivity coefficient, which can be chosen to take a larger than physically  
68 realistic value as an approximation for unresolved turbulence effects.

As bedload transport occurs along the bed and suspended sediment transport occurs across the fluid water column, the domain is conceptually divided into bedload and suspended sediment zones with an interface at  $z = z_b + \delta$  consistent with Tassi and Villaret (2014). At this interface, we define a gradient boundary condition of  $E_b = -\epsilon_s \frac{\partial c}{\partial z} |_{z=z_b+\delta} = w_s c_{b*}$  and  $D_b = w_s c_b$ , where  $E_b$  is the near-bed sediment erosion flux,  $D_b$  the deposition flux. As  $\delta$  is assumed to be small, following standard practice, the boundary condition is applied at  $z = z_b$ . Therefore, depth-averaging Eq. (4), using the boundary conditions, combining the diffusion and dispersion effects, and recalling we are modelling a long-term sedimentation process, we obtain

$$\frac{\partial}{\partial t} (h\bar{c}) + \frac{\partial}{\partial x} (h\bar{u}_1 \bar{c}) + \frac{\partial}{\partial y} (h\bar{u}_2 \bar{c}) = \frac{\partial}{\partial x} \left[ h \left( \epsilon_s \frac{\partial \bar{c}}{\partial x} \right) \right] + \frac{\partial}{\partial y} \left[ h \left( \epsilon_s \frac{\partial \bar{c}}{\partial y} \right) \right] + E_b - D_b. \quad (5)$$

Due to the coupled nature of our model, we cannot calculate  $\bar{\mathbf{u}}\bar{c}$ , but only the product of  $\bar{\mathbf{u}}$  (from the hydrodynamic component) and  $\bar{c}$  (from the sediment transport component). These two quantities are not equal because the product of two integrated variables is not equal to the integral of their product. Thus, following Huybrechts, Villaret and Hervouet (2010), we rewrite Eq. (5) as an advection-diffusion equation for  $\bar{c}$

$$\frac{\partial}{\partial t} (h\bar{c}) + \frac{\partial}{\partial x} (h\mathbf{u}_{adv_1} \bar{c}) + \frac{\partial}{\partial y} (h\mathbf{u}_{adv_2} \bar{c}) = \frac{\partial}{\partial x} \left[ h \left( \epsilon_s \frac{\partial \bar{c}}{\partial x} \right) \right] + \frac{\partial}{\partial y} \left[ h \left( \epsilon_s \frac{\partial \bar{c}}{\partial y} \right) \right] + E_b - D_b, \quad (6)$$

with advection velocity

$$\mathbf{u}_{adv} = \frac{\bar{\mathbf{u}}\bar{c}}{\bar{c}}. \quad (7)$$

We then use a correction factor  $F_{corr} = \mathbf{u}_{adv}/\bar{\mathbf{u}}$  to convert  $\bar{\mathbf{u}}$  into  $\mathbf{u}_{adv}$ . Continuing to follow Huybrechts, Villaret and Hervouet (2010), if we assume  $\mathbf{u}$  has a logarithmic profile and  $c$  has a Rouse concentration profile, we obtain

$$F_{corr} = \frac{I_2 - \log\left(\frac{B}{30}\right) I_1}{I_1 \log\left(\frac{eB}{30}\right)}, \quad (8)$$

where

$$I_1 = \int_{B^{-1}}^1 \left( \frac{(1-a)}{a} \right)^R da, \quad (9a)$$

$$I_2 = \int_{B^{-1}}^1 \log a \left( \frac{(1-a)}{a} \right)^R da, \quad (9b)$$

with  $a = z/h$ ,  $B = h/k'_s$ , where  $k'_s = 3d_{50}$  is the grain roughness coefficient, and  $R = w_s/\kappa u_*$  the Rouse number, where  $\kappa$  the Von Kármán constant (given as 0.4 in Wu, 2007) and  $u_*$  the shear velocity. To avoid numerical integration, the Rouse concentration profile is simplified, such that Eq. (9) becomes

$$I_1 = \begin{cases} \frac{1}{1-R} (1 - B^{1-R}), & R \neq 1, \\ -\log(B), & R = 1, \end{cases} \quad (10a)$$

$$I_2 = \begin{cases} \frac{I_1 + \log(B)B^{1-R}}{R-1}, & R \neq 1, \\ -0.5(\log(B))^2, & R = 1. \end{cases} \quad (10b)$$

Finally, the sediment concentration equation is

$$\frac{\partial}{\partial t}(h\bar{c}) + \frac{\partial}{\partial x}(hF_{\text{corr}}\bar{u}_1\bar{c}) + \frac{\partial}{\partial y}(hF_{\text{corr}}\bar{u}_2\bar{c}) = \frac{\partial}{\partial x}\left[h\left(\epsilon_s\frac{\partial\bar{c}}{\partial x}\right)\right] + \frac{\partial}{\partial y}\left[h\left(\epsilon_s\frac{\partial\bar{c}}{\partial y}\right)\right] + E_b - D_b. \quad (11)$$

## 69 2.2. Suspended Sediment Transport

To fully describe Eq. (11), we calculate the sediment source term,  $E_b - D_b$ , where  $E_b$  is the erosion flux and  $D_b$  the deposition flux. From the gradient boundary condition, we recall that

$$E_b - D_b = w_s c_{b*} - w_s c_b = w_s c_{b*} - w_s \alpha_c \bar{c}, \quad (12)$$

where  $w_s$  is the settling velocity of the particles,  $c_{b*}$  the equilibrium near-bed sediment concentration,  $c_b = \alpha_c \bar{c}$  the actual near-bed sediment concentration, and  $\alpha_c$  a coefficient greater than 1 which accounts for the near-bed sediment concentration value being higher than  $\bar{c}$  due to gravity. We choose to approximate  $\alpha_c$  using the following formula derived in Tassi and Villaret (2014),

$$\frac{1}{\alpha_c} = \begin{cases} \left| \frac{A(1-A^r)}{r} \right|, & |R-1| > 10^{-4}, \\ |-A \log(A)|, & |R-1| \leq 10^{-4}, \end{cases} \quad (13)$$

where

$$r = \begin{cases} \min(R-1, 3), & |R-1| > 10^{-4}, \\ 0, & |R-1| \leq 10^{-4}, \end{cases} \quad (14)$$

70  $A = \max\left(\frac{\delta}{h}, 1\right)$ ,  $R$  the Rouse number, and  $\delta$  the height of the bedload zone.

We calculate  $w_s$  in Eq. (12) using the formula defined in Van Rijn (1984)

$$w_s = \begin{cases} \frac{g\Delta d_{50}^2}{18\nu}, & d_{50} \leq 10^{-4}, \\ \frac{10\nu}{d_{50}} \left( \sqrt{1 + 0.01 \frac{g\Delta d_{50}^3}{\nu^2}} - 1 \right), & 10^{-4} \leq d_{50} \leq 10^{-3}, \\ 1.1 \sqrt{g\Delta d_{50}}, & d_{50} > 10^{-3}, \end{cases} \quad (15)$$

where  $d_{50}$  is the median sediment diameter,  $\nu$  the kinematic molecular viscosity, and

$$\Delta = \frac{\rho_s}{\rho_f} - 1, \quad (16)$$

71 where  $\rho_s$  is the sediment density, and  $\rho_f$  the water density.

As discussed in Garcia and Parker (1991), there are alternative formulae for  $c_{b*}$  in Eq. (12). Here we use the van Rijn formula which is applicable for fine sediments when no waves are present and is given in Van Rijn (1984) as

$$c_{b*} = 0.015 \frac{d_{50} S_0^{3/2}}{\delta d_*^{3/10}}, \quad (17)$$

where  $d_*$  is the non-dimensional diameter

$$d_* = d_{50} \left( \frac{g\Delta}{\nu^2} \right)^{1/3}, \quad (18)$$

and  $S_0$  the transport stage parameter

$$S_0 = \frac{\Psi \tau_b - \tau_c}{\tau_c}. \quad (19)$$

See Tassi and Villaret (2014) for more detail. In Eq. (19),  $\tau_c$  is the critical shear stress

$$\tau_c = (\rho_s - \rho_f) g d_{50} \theta_{cr}, \quad (20)$$

where  $\theta_{cr}$  is the critical shields parameter;  $\tau_b$  is the bed shear stress acting against the velocity flow and equal in magnitude in both directions

$$\tau_b = \frac{1}{2} \rho_f C_h (\bar{u}_1^2 + \bar{u}_2^2), \quad (21)$$

where  $(\bar{u}_1, \bar{u}_2)$  is the depth-averaged velocity; and  $\Psi$  is the skin friction correction

$$\Psi = \frac{2\kappa^2}{C_h \left[ \log \left( \frac{11.036h}{k'_s} \right) \right]^2}, \quad (22)$$

where  $C_h$  is the Nikuradse quadratic drag coefficient

$$C_h = 2 \frac{\kappa^2}{\log \left( \frac{11.036h}{k_s} \right)^2}, \quad (23)$$

72 where  $k_s$  is the Nikuradse friction height.

73 The actual skin friction is implemented using Eq. (23) but with  $k_s$  replaced by  $k'_s$  (as in Tassi and Villaret, 2014).

### 74 2.3. Bedload transport

Following Tassi and Villaret (2014), for modelling bedload transport we define the bedload transport flux,  $\mathbf{Q}_b$

$$\mathbf{Q}_b = \phi_s \sqrt{g \left( \frac{\rho_s}{\rho_f} - 1 \right)} d_{50}^3 (\cos \xi, \sin \xi), \quad (24)$$

where  $\cos \xi = \frac{\bar{u}_1}{\sqrt{\bar{u}_1^2 + \bar{u}_2^2}}$  and  $\sin \xi = \frac{\bar{u}_2}{\sqrt{\bar{u}_1^2 + \bar{u}_2^2}}$ . We choose the Meyer-Peter-Müller formula to define the non-dimensional sediment rate  $\phi_s$

$$\phi_s = \begin{cases} 0, & \theta' < \theta_{cr}, \\ \alpha_{MPM} (\theta' - \theta_{cr})^{3/2}, & \text{otherwise,} \end{cases} \quad (25)$$

where  $\theta_{cr}$  is the critical shields parameter,  $\alpha_{MPM}$  a coefficient equal to 8, as suggested by Tassi and Villaret (2014), and  $\theta'$  the non-dimensional shields parameter

$$\theta' = \frac{\Psi \tau_b}{(\rho_s - \rho_f) g d_{50}}, \quad (26)$$

75 with  $\Psi$  given by Eq. (19) and  $\tau_b$  by Eq. (21).

#### 76 2.3.1. Slope effect

77 In practice, the magnitude and direction of  $\mathbf{Q}_b$  depends on the gradient of the bed, but this is not reflected in Eq.  
78 (24). When the bed has a positive gradient in the transport direction, gravity acts against the sediment causing the  
79 magnitude of  $\mathbf{Q}_b$  to decrease and its direction to alter, and vice versa for a negative gradient.

80 (i) *Magnitude correction*

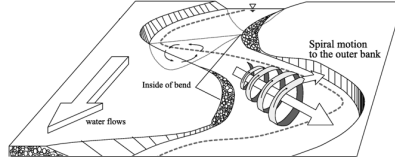


**Figure 1:** Secondary current in curved channel, adapted from Park and Ahn (2019).

To correct the magnitude we use

$$\mathbf{Q}_{b*} = \mathbf{Q}_b \left( 1 - \Upsilon \frac{\partial z_b}{\partial s} \right), \quad (27)$$

81 given in Soulsby (1997), where  $s$  is a direction tangential to the current and  $\Upsilon$  an empirical coefficient set to 1.3 (Tassi  
82 and Villaret, 2014).

83 (ii) *Angle correction*

To correct the angle, following Talmon, Struiksmas and Mierlo (1995), we set

$$T = \frac{1}{\beta_2 \sqrt{\theta}}, \quad (28)$$

where  $\beta_2$  is an empirical coefficient (equal to 1.5 for river test cases) and  $\theta$  is given by

$$\theta = \frac{(\rho_f - \rho_s) g d_{50}}{\max\left(\frac{1}{2} \rho_f C_h \|\bar{\mathbf{u}}\|^2, 10^{-10}\right)}, \quad (29)$$

with  $C_h$  defined as in Eq. (23). Thus

$$\mathbf{Q}_b = \left( \phi_s \sqrt{g \left( \frac{\rho_s}{\rho_f} - 1 \right) d_{50}^3} (\cos \alpha, \sin \alpha) \right), \quad (30)$$

where  $\alpha$  is the corrected angle defined by

$$\begin{pmatrix} \sin \alpha \\ \cos \alpha \end{pmatrix} = \frac{1}{\|\mathbf{p}\|^2} \begin{pmatrix} p_1 \\ p_2 \end{pmatrix} = \frac{1}{\|\mathbf{p}\|^2} \begin{pmatrix} \sin \xi - T \left( \frac{\partial z_b}{\partial y} \right) \\ \cos \xi - T \left( \frac{\partial z_b}{\partial x} \right) \end{pmatrix}, \quad (31)$$

84 where  $\mathbf{p} = (p_1, p_2)$ .

### 85 2.3.2. Secondary current

As shown in Figure 1, depth-averaged models for curved channels need to account for both the current and a helical flow effect. This affects the magnitude and direction of  $\mathbf{Q}_b$  and in Tassi and Villaret (2014) is implemented on top of slope effect corrections. Therefore, we implement a secondary current using

$$\tan \zeta = 7 \frac{h}{r}, \quad (32)$$

given in Engelund (1974), where  $\zeta$  is the angle between the bedload transport and the main flow direction,  $h$  the mean water depth, and  $r$  the local radius of curvature of the streamline calculated using

$$r = \frac{\alpha' (\bar{u}_1^2 + \bar{u}_2^2)}{g \frac{\partial \eta}{\partial n}}, \quad (33)$$

86 where  $\eta$  is the elevation,  $n$  a direction normal to the current and  $\alpha'$  a coefficient which lies between 0.75 (rough bed)  
87 and 1 (smooth bed).

Using Eq. (32), we construct the term

$$\Xi = \sqrt{(\tau_b \Upsilon \cos \alpha + \tau_b \bar{u}_2 \tan \zeta)^2 + (\tau_b \Upsilon \sin \alpha - \tau_b \bar{u}_1 \tan \zeta)^2}, \quad (34)$$

88 where  $\tau_b$  is the bedload shear stress defined by Eq. (21), and  $\alpha$  and  $\Upsilon$  are the corrected flow angle and magnitude  
89 factors (Section 2.3.1).

Hence, we define a new corrected bed transport flow direction  $\hat{\alpha}$  with

$$\cos \hat{\alpha} = \frac{\tau_b \Upsilon \cos \alpha + \tau_b \bar{u}_2 \tan \zeta}{\Xi}, \quad (35a)$$

$$\sin \hat{\alpha} = \frac{\tau_b \Upsilon \sin \alpha - \tau_b \bar{u}_1 \tan \zeta}{\Xi}, \quad (35b)$$

and a new slope magnitude correction factor

$$\hat{\Upsilon} = \frac{\Xi}{\tau_b}. \quad (36)$$

90 Note that if a secondary current effect is imposed without slope effect corrections, then  $\Upsilon = 1$  and  $\alpha = \xi$ , *i.e.* the  
91 original flow angle.

## 92 2.4. Calculating the new bedlevel

The new bedlevel,  $z_b$ , is affected by both the suspended sediment and bedload transport described in Sections 2.2  
and 2.3, and is governed by the Exner equation

$$(1 - p') \frac{dz_b}{dt} + \nabla_h \cdot \mathbf{Q}_b = D_b - E_b, \quad (37)$$

93 where  $p'$  is the bed sediment porosity. This completes the model equations.

## 94 2.5. Practical application within the *Thetis* framework

95 When implementing our model, we use two common techniques for algorithm stability and efficiency reasons.

### 96 2.5.1. *Spinning up the hydrodynamics*

97 Once the simulation starts, we are forcing a previously motionless flow, and the resulting flow instabilities could  
98 trigger unrealistic bedlevel changes. Following standard practice (e.g. Gerritsen et al., 2008), we avoid this by first  
99 running a simulation solving only the hydrodynamic equations. When the velocity and elevation fields have reached  
100 an approximate steady state, we introduce sediment and enable bedlevel changes.

### 101 2.5.2. *Morphological scale factor*

Once running a bed evolution simulation for a long period of time, a morphological scale factor,  $m$ , is often used  
(e.g. Gerritsen et al., 2008) which increases the rate of bedlevel changes and saves computational time. This factor  
means that each  $\Delta t$  in the hydrodynamic and sediment concentration equations is equivalent to  $m\Delta t$  for the bed  
evolution. We implement this by including the factor  $m$  in the Exner equation (37)

$$\frac{(1 - p')}{m} \frac{dz_b}{dt} + \nabla_h \cdot \mathbf{Q}_b = D_b - E_b. \quad (38)$$

102 This factor is suitable because the hydrodynamics are in an approximate steady state, and we assume throughout that  
103 changes in the bed are significantly slower than in the hydrodynamics.

## 104 3. Finite element based implementation

105 We build on existing elements of *Thetis* for the implementation of a coupled hydrodynamic and sediment transport  
106 model. *Thetis* is a finite element coastal ocean modelling system (built using the code generating framework *Fire Drake*)  
107 which is first described in Kärnä et al. (2018) with a 3D model. We use the 2D depth-averaged version of *Thetis* outlined  
108 in Vouriot et al. (2019), which solves the shallow water equations and the non-conservation form of a depth-averaged  
109 sediment concentration equation, as discussed in the previous section.

110 We use a discontinuous Galerkin based finite element discretisation (DG) which has several advantages in this  
111 context, as discussed in Section 1.

### 112 3.1. DG based methods in *Thetis*

When using DG based methods, we generate an unstructured mesh of triangular elements tessellating our domain  $\Omega$  and then define our finite element space on this mesh. Using a discontinuous function space requires the definition of variables on element edges (including on the domain boundary  $d\Omega$ ), with the union of these edges denoted by  $\Gamma$ . The average operator  $\{\{\cdot\}\}$  and jump operator  $[[\cdot]]$  across the interior edges on scalar and vector fields are

$$\begin{aligned} \{\{\mathbf{X}\}\} &= \frac{1}{2}(\mathbf{X}^+ + \mathbf{X}^-), & [[\chi]]_{\mathbf{n}} &= \chi^+ \mathbf{n}^+ + \chi^- \mathbf{n}^-, \\ [[\mathbf{X}]]_{\mathbf{n}} &= \mathbf{X}^+ \cdot \mathbf{n}^+ + \mathbf{X}^- \cdot \mathbf{n}^-, \end{aligned}$$

113 where  $\mathbf{n} = (n_x, n_y, 0)$  is the horizontal projection of the outward pointing unit normal on the element edge, and ‘+’ and  
114 ‘-’ denote either side of the interior edge.

#### 115 3.1.1. Depth-averaged sediment concentration equation

*Thetis* uses very similar techniques to solve the hydrodynamic equations, (1) and (2), and the sediment concentration equation (11). We focus on the latter because it is the most pertinent for this work; the formulation for the hydrodynamic equations can be found in Kärnä et al. (2018), Pan, Kramer and Piggott (2019) and Vouriot et al. (2019). In the advection term, *Thetis* uses an upwinding scheme for the sediment concentration,  $\bar{c}$ : at each edge,  $\bar{c}$  is chosen to be equal to its upstream value with respect to velocity,  $\bar{c}^{\text{up}}$  (see Leveque, 1996). Hence, the weak form of the advection term  $\bar{\mathbf{u}} \cdot \nabla_h \bar{c}$  in Eq. (11) is

$$\int_{\Omega} \psi \bar{\mathbf{u}} \cdot \nabla_h \bar{c} dx = - \int_{\Omega} \bar{c} \nabla_h \cdot (\bar{\mathbf{u}} \psi) dx + \int_{\Gamma} \bar{c}^{\text{up}} [[\psi \bar{\mathbf{u}}]]_{\mathbf{n}} ds. \quad (39)$$

Following Kärnä et al. (2018), we must apply a stabilisation method to the weak form of the diffusivity term,  $-\nabla_h \cdot (\epsilon_s \nabla_h \bar{c})$ , to ensure the discretisation is stable for elliptic operators. We use the Symmetric Interior Penalty Galerkin (SIPG) method given in Epshteyn and Rivière (2007), with the penalty parameter  $\sigma$  given in Kärnä et al. (2018). Hence, the weak form of the diffusivity term is

$$- \int_{\Omega} \psi \nabla_h \cdot (\epsilon_s \nabla_h \bar{c}) dx = \int_{\Omega} \epsilon_s (\nabla_h \psi) \cdot (\nabla_h \bar{c}) dx - \int_{\Gamma} [[\psi]]_{\mathbf{n}} \cdot \{\{\epsilon_s \nabla_h \bar{c}\}\} ds - \int_{\Gamma} [[\bar{c}]]_{\mathbf{n}} \cdot \{\{\epsilon_s \nabla_h \psi\}\} ds + \int_{\Gamma} \sigma \{\{\epsilon_s\}\} [[\bar{c}]]_{\mathbf{n}} \cdot [[\psi]]_{\mathbf{n}} ds. \quad (40)$$

The use of upwinded numerical fluxes and slope limiters makes our model robust for modelling the steep bed gradients formed (see Kubatko, Westerink and Dawson, 2006). Finally, the weak form of the sediment transport source term,  $E_b - D_b$ , is simply

$$\int_{\Omega} (\text{Source Term}) \psi dx = \int_{\Omega} (E_b - D_b) \psi dx. \quad (41)$$

We use the implicit backward Euler method to proceed from the  $n^{\text{th}}$  to the  $(n+1)^{\text{th}}$  timestep in Eq. (11). Thus, the final equation is

$$\int_{\Omega} \frac{\bar{c}_i^{(n+1)} - \bar{c}_i^{(n)}}{\Delta t} \psi dx = F_i^{(n+1)}, \quad (42)$$

116 where  $F_i^{(n+1)}$  is the sum of the weak forms (39), (40) and (41). The combination of a DG based method with an implicit  
117 timestepping method makes our model more robust.

#### 118 3.1.2. Exner Equation

In order to avoid grid-scale noise and unstable oscillations when solving the Exner equation (37), we define the bedlevel,  $z_b$ , on a continuous grid, and thus use a continuous Galerkin based finite element discretisation (CG). We project all hydrodynamic and sediment transport variables from the DG space into the CG space before calculating the terms in the Exner equation. This causes a very slight loss of accuracy in our model variables, but overall a more stable bedlevel result. The weak form of the divergence term  $\nabla_h \cdot \mathbf{Q}_b$  is

$$\int_{\Omega} \psi \nabla_h \cdot \mathbf{Q}_b dx = - \int_{d\Omega} (\mathbf{Q}_b \cdot \mathbf{n}) \psi ds + \int_{\Omega} (\mathbf{Q}_b \cdot \nabla_h) \psi dx. \quad (43)$$



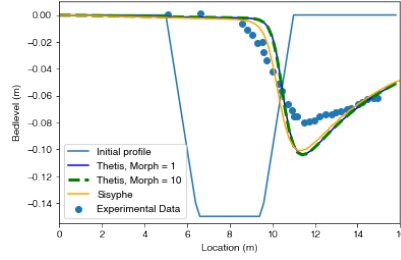


**Figure 2:** Bedlevel after 15 h for different morphological scale factors comparing experimental data, *Sisyphé* and *Thetis* with  $\Delta t = 0.05$  s. Experimental data and initial trench profile source: Villaret et al. (2016).

On a continuous grid and assuming centred fluxes on interior edges, the values on either side of each interior edge cancel over the whole domain, meaning that the only boundary contribution is from the domain boundary,  $d\Omega$ . We use the implicit backward Euler method to solve Eq. (37) allowing us to use large timesteps stably. Thus

$$\int_{\Omega} \left( (1 - p') \frac{z_{b_i}^{(n+1)} - z_{b_i}^{(n)}}{\Delta t} \right) \psi dx = G_i^{(n+1)}, \quad (44)$$

119 where  $G_i^{(n+1)}$  is the sum of the weak forms (41) and (43). Note that the radius of curvature, (33), in the secondary  
 120 current parametrisation is dependent on the surface elevation  $\eta$  rather than on  $z_b$ . Hence, we rewrite  $\eta$  as  $(h + z_b)$   
 121 meaning we can benefit from an implicit discretisation.

## 122 4. Migrating trench test case

123 In this section, we consider the simple test case of a migrating trench (as in, for example, Gerritsen et al. 2008 and  
 124 Van Rijn 1980). We use this test case to validate the implementation of the mathematical and numerical methods used  
 125 in *Thetis* by using experimental data from a lab study in Van Rijn (1980) and results from Villaret et al. (2016).

126 In Villaret et al. (2016), for this test case, a coupled model is used comprising of Telemac-Mascaret's 2D depth-  
 127 averaged hydrodynamic module, Telemac2D, and its sediment transport and bed evolution module, *Sisyphé*. Hereafter  
 128 in this work, we refer to this coupled model as *Sisyphé*. For the discretisation, they use Telemac-Mascaret's continuous  
 129 finite element model (Danilov, 2013) with the method of characteristics for the hydrodynamic advection terms and  
 130 distributive schemes for the sediment transport advection terms. The method of characteristics has the advantage of  
 131 being unconditionally stable, but is not mass conservative and is diffusive for small timesteps, meaning the problem  
 132 is artificially regularised with potentially spurious mixing. Distributive schemes are mass conservative, but also have  
 133 high numerical diffusion and Courant number limitations to ensure stability. For further details on both methods, see  
 134 Hervouet (2007) and Tassi and Villaret (2014). The limitations of these two methods in part motivate our use of DG  
 135 based methods in *Thetis*.

### 136 4.1. Test case configuration

137 In Figure 2, the initial trench profile and the final bedlevel profile after a 15 h experiment is observed demonstrating  
 138 the trench migration over time.

139 For *Sisyphé*, we use the model of Villaret et al. (2016), and summarise the parameter values in Table 1. As these  
 140 have been calibrated and the model validated by experiments, *Sisyphé*'s results can assist the validation of our model.  
 141 Thus, we use the same parameter values in *Thetis*. We also use a grid with a mesh size of  $\Delta x = 0.2$  m in the  $x$ -direction  
 142 and of  $\Delta y = 0.22$  m in the  $y$ -direction. Villaret et al. (2016) use a finer  $\Delta y$  of 0.11 m, but we find our *Thetis* results  
 143 are consistent with either  $\Delta y$ , and thus adopt the least computationally expensive option. Finally, we use the boundary  
 144 conditions from Section 2 and set the incoming suspended sediment flow rate so that the erosion flux,  $E_b$ , equals the  
 145 deposition flux,  $D_b$ , at the upstream boundary. Hence, we have sediment equilibrium and the bed remains unaltered at  
 146 the inlet.

### 147 4.2. Results

148 In this section, we run both *Thetis* and *Sisyphé* for this test case. As discussed in Section 2.5, we first run a pure  
 149 hydrodynamics simulation for 200 s ramping up the initial hydrodynamic conditions for our coupled simulation with

**Table 1**

Parameter values for the migrating trench test case Villaret et al. (2016)

Variable Name	Variable Value
Length in $x$ -direction	16 m
Length in $y$ -direction	1.1 m
Morphological simulation time	15 h
Depth	0.397 m
Downstream elevation	0.4 m
Upstream flux	$0.22 \text{ m}^3 \text{ s}^{-1}$
Median particle size ( $d_{50}$ )	$1.6 \times 10^{-4} \text{ m}$
Sediment density ( $\rho_s$ )	$2650 \text{ kg m}^{-3}$
Water density ( $\rho_f$ )	$1000 \text{ kg m}^{-3}$
Kinematic viscosity ( $\nu$ )	$1 \times 10^{-6} \text{ m}^2 \text{ s}^{-1}$
Bed sediment porosity ( $p'$ )	0.4
Diffusivity ( $\epsilon_s$ )	$0.01 \text{ m}^2 \text{ s}^{-1}$
Nikuradse friction height ( $k_s$ )	0.025 m

150 bedload and suspended sediment transport. We do not use either the slope effect angle correction or secondary current  
 151 here because both are superfluous in a straight channel.

152 Figure 2 shows that the bedlevel results from *Thetis* and *Sisyphé* agree in both magnitude and profile, but are clearly  
 153 different from the experimental data. By contrast, when Villaret et al. (2016) use the parameter values in Table 1, the  
 154 *Sisyphé* results agree with the experimental data. The difference between the two set-ups is the timestep,  $\Delta t$ : Villaret  
 155 et al. (2016) use  $\Delta t = 1 \text{ s}$ , whereas we use  $\Delta t = 0.05 \text{ s}$  in Figure 2. This choice of  $\Delta t$  is because *Thetis* requires a  
 156 smaller Courant number ( $U \Delta t / \Delta x$ ) than *Sisyphé* and for comparability reasons the same  $\Delta t$  is used in both models.  
 157 A possible explanation of this Courant number requirement in *Thetis* is that the overall model can be perceived as  
 158 semi-implicit since all model equations are solved implicitly, while the coupling of the hydrodynamic and sediment  
 159 transport components is explicit.

160 Figure 2 also illustrates that using either a morphological scale factor of 10 or 1 in our *Thetis model* gives very  
 161 similar results. Unless otherwise stated all figures in this section are produced using a morphological scale factor of  
 162 10. Although *Sisyphé* has an option for a morphological scale factor, it is not imposed in this work in *Sisyphé* because  
 163 neither Villaret et al. (2016) or Villaret et al. (2013) apply it.

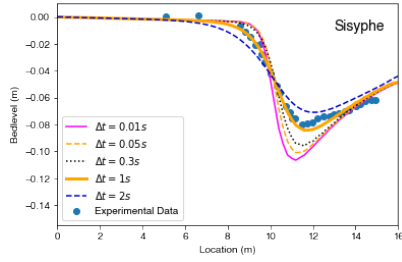
#### 164 4.2.1. Sensitivity study

165 The dependence of *Sisyphé*'s results on  $\Delta t$  suggests this test case would benefit from a sensitivity study on the  
 166 robustness of the models to small changes in physical parameters, timestep and/or mesh step size. First, we explore  
 167 the impact of varying  $\Delta t$  and the mesh size  $\Delta x$  on the final bedlevel. Note that the mesh size  $\Delta y$  has no effect because  
 168 there is negligible bedlevel variation in that direction. Figure 3a shows that the *Sisyphé* bedlevel results vary signifi-  
 169 cantly with  $\Delta t$ . Only when  $\Delta t = 1 \text{ s}$ , the value of Villaret et al. (2016), is there agreement between *Sisyphé* and the  
 170 experimental data. As  $\Delta t$  decreases, *Sisyphé*'s results converge to the same result as *Thetis* in Figure 2. By contrast,  
 171 bedlevel results from *Thetis* are largely insensitive to changes in  $\Delta t$ , as seen in Figure 3b. Figures 3b, 3c and 3d show  
 172 how both models are relatively insensitive to changes in  $\Delta x$  for this test case.

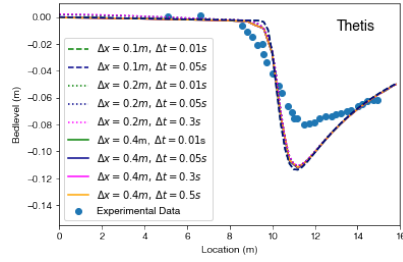
173 *Thetis* produces robust and accurate results for small Courant numbers, but not for large values, unlike *Sisyphé* (as  
 174 discussed earlier in this subsection). This prevents us from comparing the two models for every  $\Delta x$  and  $\Delta t$  combination  
 175 run in *Sisyphé*. However, although *Sisyphé* is stable for larger values of  $\Delta t$ , the results it produces for these values are  
 176 not timestep convergent and show significant variability.

177 Furthermore, we run a small study to investigate whether *Sisyphé* is always sensitive to  $\Delta t$  for this test case. When  
 178 the method of characteristics is chosen for the hydrodynamics, as in Villaret et al. (2016), we find *Sisyphé* is always  
 179 sensitive to  $\Delta t$ , independent of the choice of morphodynamic scheme. Other methods for the hydrodynamics have  
 180 stricter Courant number criteria, requiring  $\Delta t < 0.01 \text{ s}$  to run (even smaller than our *Thetis* value), meaning this effect  
 181 is less noticeable.

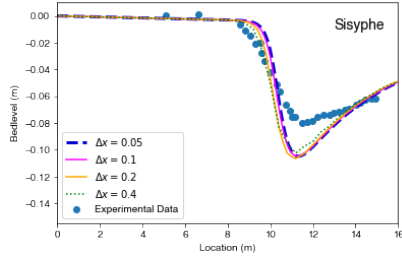
182 For small values of  $\Delta t$ , *Thetis* and *Sisyphé* are consistent. We conjecture that the errors caused in *Sisyphé* with  
 183 larger  $\Delta t$  values manifest themselves as an increase in effective diffusivity in the model. We thus conduct a sensitivity  
 184 study for the sediment turbulent diffusivity coefficient,  $\epsilon_s$ . For this study, we choose  $\Delta t = 0.05 \text{ s}$  in both models because  
 185 *Sisyphé* is close to convergence for this value, at a relatively small computational time (approximately 50 min). Bedlevel  
 186 results from both *Sisyphé* and *Thetis* in Figures 4a and 4b show they are indeed greatly affected by  $\epsilon_s$  and, importantly,



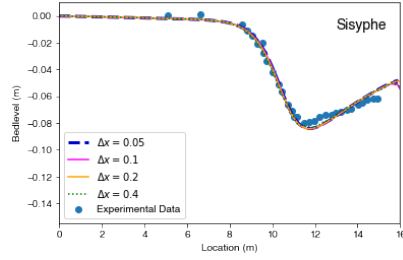
(a) Sisyphé with  $\Delta x = 0.2m$ .



(b) Thetis.

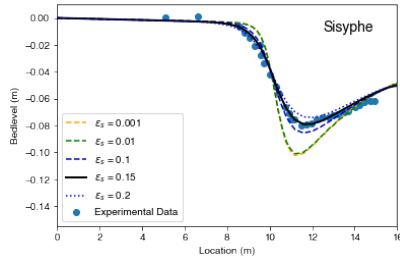


(c) Sisyphé with  $\Delta t = 0.01 s$ .

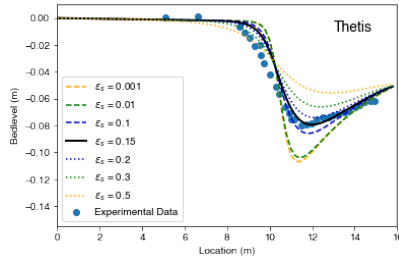


(d) Sisyphé with  $\Delta t = 1 s$ .

**Figure 3:** Sensitivity of bedlevel to  $\Delta x$  and  $\Delta t$ .



(a) Sisyphé.



(b) Thetis.

**Figure 4:** Sensitivity of bedlevel to diffusivity ( $\Delta x = 0.2m$ ,  $\Delta t = 0.05s$ ).

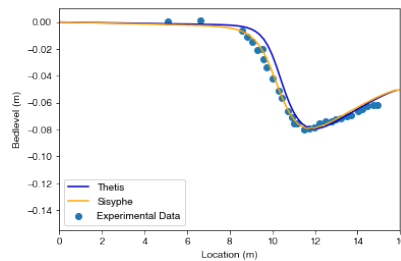


**Figure 5:** Bedlevel from *Thetis* and *Sisyphé* after 15h using  $\epsilon_s = 0.15m^2/s$  and  $\Delta t = 0.05s$ .

187 that both models behave consistently. Note that, due to stability constraints, *Sisyphé* does not run with  $\epsilon_s > 0.2 m^2 s^{-1}$ ,  
 188 unlike *Thetis*. The observed sensitivity to  $\epsilon_s$  is to be expected because the grid Peclet number ( $U\Delta x/\epsilon_s$ ) decreases  
 189 with  $\epsilon_s$ , making diffusion the key driver of the sediment concentration equation, rather than advection. Thus, we can  
 190 use  $\epsilon_s$  to calibrate both models; in *Sisyphé*,  $\Delta t$  can be used to similar effect.

191 If we set  $\epsilon_s = 0.15 m^2 s^{-1}$ , *Thetis* and *Sisyphé*'s converged results agree well with each other and with the experi-  
 192 mental data, as shown clearly in Figure 5. Thus, we have validated *Thetis* for this simple test case.

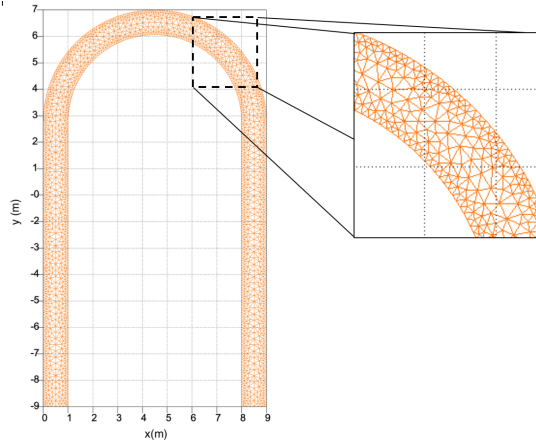


**Figure 6:** Meander mesh and domain used both in *Thetis* and *Sisyphé* by Villaret et al. (2013).

**Table 2**

Parameter values for the meander test case Villaret et al. (2013)

Variable Name	Variable Value
Channel width	1 m
Inner radius	3.5 m
Outer radius	4.5 m
Straight reach at channel ends	11.5 m
Morphological simulation time	5 h
Depth	0.0544 m
Median particle size ( $d_{50}$ )	$1 \times 10^{-3}$ m
Sediment density ( $\rho_s$ )	$2650 \text{ kg m}^{-3}$
Water density ( $\rho_f$ )	$1000 \text{ kg m}^{-3}$
Kinematic viscosity ( $\nu$ )	$0.01 \text{ m}^2 \text{ s}^{-1}$
Bed sediment porosity ( $p'$ )	0.4
Nikuradse friction height ( $k_s$ )	0.0035 m

## 193 5. Meander test case

194 Our second test case regards the curved channel of a meander, which requires and demonstrates the implemen-  
 195 tation of a slope effect angle correction and a secondary current. This test case is used to validate these additional  
 196 functionalities, and affirm our model can handle more complex and realistic set-ups.

### 197 5.1. Test case configuration

198 We use the configuration from experiment 4 from Yen and Lee (1995) and validate *Thetis* through the experimental  
 199 data and *Sisyphé* results from Villaret et al. (2013). Most of the bed changes occur at the boundary so, following Villaret  
 200 et al. (2013), we use a finer mesh there (0.1 m) and a coarser one (0.25 m) along the centre of the channel, as in Figure  
 201 6.

202 We impose time dependent flux and elevation boundary conditions reproducing Yen and Lee (1995). The initial  
 203 inflow flux and outflow elevation are  $0.02 \text{ m}^3 \text{ s}^{-1}$  and 0 m, respectively. Both increase linearly until reaching their  
 204 respective maximums of  $0.053 \text{ m}^3 \text{ s}^{-1}$  and 0.103 m at 100 min, and then decrease linearly to their initial values at 5 h.  
 205 We also impose a free-slip condition on the meander boundary walls.

206 In both *Thetis* and *Sisyphé*, we use the parameter values summarised in Table 2. Following Villaret et al. (2013),  
 207 we only model bedload transport because this is the principal sediment transport component in rivers. Hence, we do  
 208 not need to specify the diffusivity coefficient  $\epsilon_s$ . The implementation of the secondary current requires we determine  
 209 the flow roughness to set the value of  $\alpha'$  in Eq. (33). Following Kulkarni and Sahoo (2013), we calculate that the  
 210 roughness Reynolds number,  $(k_s \sqrt{\tau_b}) / (\nu \sqrt{\rho_f})$ , is approximately 80, and conclude we are in a rough turbulent flow  
 211 regime. Consistently with Tassi and Villaret (2014), we use  $\alpha' = 0.75$ .

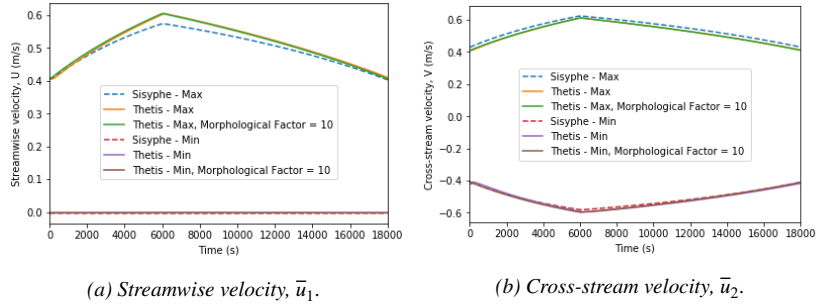


**Figure 7:** Minimum and maximum velocities from *Thetis* ( $\nu = 0.035 \text{ m}^2 \text{ s}^{-1}$ , slope = 0.0035) with a morphological scale factor of 1 and 10, and *Sisyphé* ( $\nu = 0.01 \text{ m}^2 \text{ s}^{-1}$ , slope = 0.002).

## 5.2. Results

### 5.2.1. Modelling the hydrodynamics

If we use the same viscosity value when modelling the hydrodynamics for the meander test case as for the migrating trench test case ( $1 \times 10^{-6} \text{ m}^2 \text{ s}^{-1}$ ), we find that our model does not accurately solve the flow at the meander boundary walls. Instead of finding a smooth solution, the flow magnitude increases dramatically in the cells closest to the boundary. However molecular viscosity values ( $1 \times 10^{-6} \text{ m}^2 \text{ s}^{-1}$ ) only become relevant at the Kolmogorov scale. Our test case is at a much larger scale where a viscous force exists caused by turbulence, Thus the viscosity is a turbulence or eddy viscosity and a value of  $1 \times 10^{-3} \text{ m}^2 \text{ s}^{-1}$  (the value by Vouriot et al. (2019) for their *Thetis* test case) is more appropriate. As we increase  $\nu$  in the hydrodynamic equations (1) and (2) the flow becomes smoother and for viscosity values of  $O(1 \times 10^{-3})$  the boundary issue no longer exists. The issue itself is related to how boundary conditions at closed impermeable boundaries are imposed in equal order DG discretisations and will be addressed in the future.

As we are not using a turbulence model, to find the correct value of  $\nu$ , we use *Sisyphé*'s hydrodynamic results to calibrate our model, noting that Villaret et al. (2013) use  $1 \times 10^{-2} \text{ m}^2 \text{ s}^{-1}$ . These alterations in  $\nu$  change the nature of the test case, but can be balanced by altering the longitudinal bed slope. In Yen and Lee (1995), the meander has a longitudinal bed slope of 0.002, as in Villaret et al. (2013). We find that if we set the longitudinal bed slope to 0.0035 and  $\nu$  to  $0.035 \text{ m}^2 \text{ s}^{-1}$ , our model's velocities match those in *Sisyphé* reasonably well, as shown in Figures 7a and 7b. These figures also show that even with time dependent boundary conditions, using a morphological scale factor equal to either 1 or 10 in *Thetis* gives equivalent results. Thus, unless otherwise stated, in this section our *Thetis* results are produced with a morphological scale factor of 10.

### 5.2.2. Modelling sediment transport

As the hydrodynamic flow of *Thetis* agrees with *Sisyphé*, we introduce sediment transport into the models. As discussed in Section 2.5, we first run a simulation for 200 s solving only the hydrodynamics with a fixed flux inflow of  $0.02 \text{ m}^3 \text{ s}^{-1}$  and outflow elevation of 0 m. For our full sediment transport simulation, we use these results as the initial hydrodynamic conditions and impose time dependent flux and elevation conditions from Section 5.1 as the boundary conditions. We present the scaled bedlevel evolution results which is defined as

$$\text{Scaled Bedlevel Evolution} = \frac{z_{\text{final}} - z_{\text{initial}}}{z_{\text{initial}}} \quad (45)$$

where  $z_{\text{final}}$  is the final bedlevel after 5 h and  $z_{\text{initial}}$  is the initial bedlevel of  $-0.0544 \text{ m}$ .

Figure 8 shows the effects of implementing secondary current and slope effects on the bedlevel evolution at the meander outflow. The slope effect magnitude correction has little effect compared to the secondary current and slope effect angle corrections, likely because the slopes in this test case are fairly gentle.

In Figure 8d, the final scaled bedlevel evolution result is shown, with erosion at the outer bend and deposition at the inner bed, as expected from physical intuition. Comparing this figure with Figure 9, we see *Thetis* result has the same distribution and magnitude as the experiment and *Sisyphé*. Hereafter, unless otherwise stated, all *Sisyphé* results are those presented in Villaret et al. (2013).

To compare our *Thetis* result with the experiment and *Sisyphé*'s results more accurately, we take a cross-section at the  $90^\circ$  and  $180^\circ$  angles marked on Figure 9. Figures 10a and 10b show our model approximates the experimental

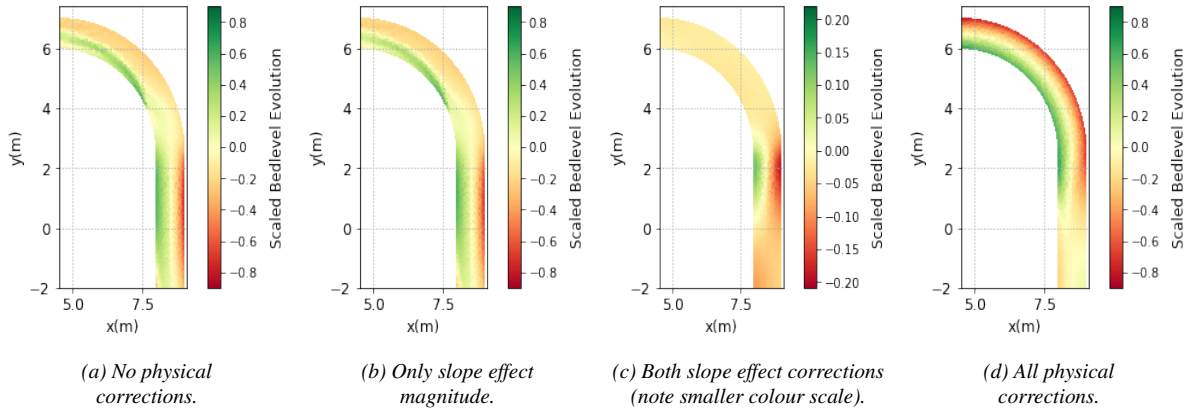


**Figure 8:** Meander section showing scaled bedlevel evolution from *Thetis* with different physical corrections to  $Q_b$ .

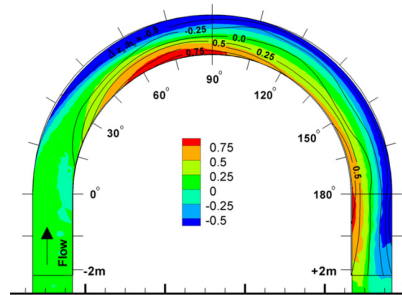


**Figure 9:** Scaled bedlevel evolution from *Sisyphé* (coloured bars) and experimental data (black contours). Source: Villaret et al. (2013).

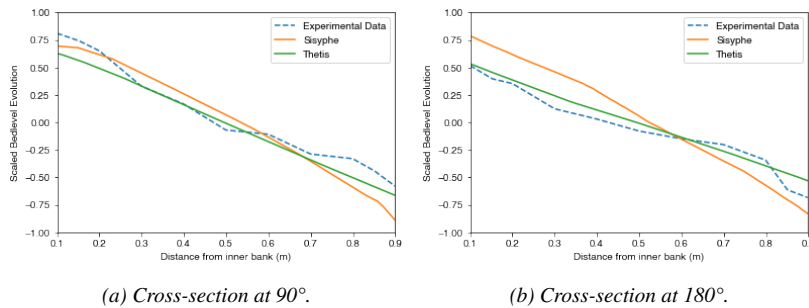


**Figure 10:** Scaled bedlevel evolution from *Thetis* (with  $\nu = 0.035 \text{ m}^2 \text{ s}^{-1}$ , slope = 0.0035), *Sisyphé* Villaret et al. (2013) and experimental data Yen and Lee (1995).

242 results better than *Sisyphé*, with a particular improvement at the 180° cross-section and in the bedlevel erosion at both  
 243 cross-sections.

### 244 5.2.3. Calibration study

In Section 5.2.1, we used the hydrodynamic results from *Sisyphé* to calibrate the viscosity and longitudinal slope in *Thetis* because those from the experiment are not available. However, Figures 10a and 10b show *Sisyphé* does not agree completely with the experimental data. Hence, to improve our model's accuracy, we re-run the calibration study this time using the experimental data as the 'real solution'. We seek to minimize the relative error norm at both the

**Table 3**

Sum of relative error norms for different values of longitudinal slope and  $\nu$  ( $\text{m}^2 \text{s}^{-1}$ ).

Slope	$\nu = 0.025$	$\nu = 0.035$	$\nu = 0.05$	$\nu = 0.075$
0.003	0.5041	0.4934	0.4847	0.4930
0.0035	0.4911	0.4828	0.4752	0.4851
0.004	0.5253	0.5167	0.5106	0.5199
0.0045	0.5809	0.5707	0.5635	0.5686

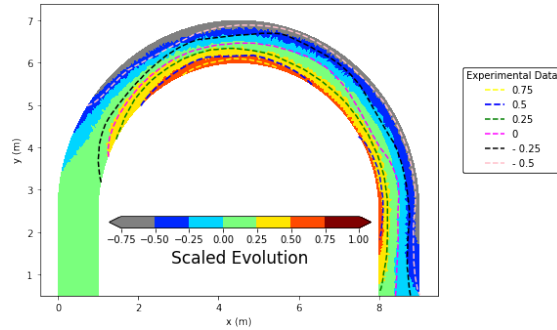


**Figure 11:** Scaled bedlevel evolution from *Thetis* with  $\nu = 0.05 \text{ m}^2 \text{ s}^{-1}$ , slope = 0.0035 and experimental data Yen and Lee (1995).

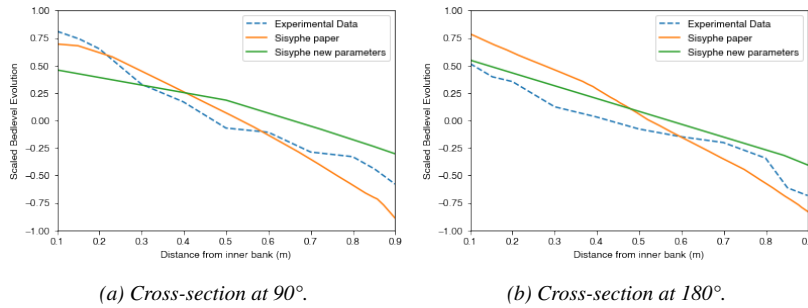


**Figure 12:** Scaled bedlevel evolution from *Sisyphé* in Villaret et al. (2013), *Sisyphé* with  $\nu = 0.05 \text{ m}^2 \text{ s}^{-1}$  and slope = 0.0035, and experimental data Yen and Lee (1995).

90° and 180° cross-section and thus minimise

$$\frac{\|y_{90_i} - \hat{y}_{90_i}\|_2}{\|\hat{y}_{90_i}\|_2} + \frac{\|y_{180_i} - \hat{y}_{180_i}\|_2}{\|\hat{y}_{180_i}\|_2}, \quad (46)$$

245 where  $\hat{y}_i$  is the experimental data and  $y_i$  our model result. The results are given in Table 3. Hence, we conclude that  
 246 a viscosity of  $0.05 \text{ m}^2 \text{ s}^{-1}$  and a longitudinal slope of 0.0035 yield the best approximation to the experimental data.  
 247 For these values, Figure 11 shows that the scaled bedlevel evolution from *Thetis* agrees closely with the experiment,  
 248 particularly at the inner bend and at the meander outflow. Comparing the experiment, *Sisyphé* results in Figure 9 and  
 249 our results in Figure 11, we see that *Thetis* predicts the bedlevel erosion to a greater degree of accuracy, particularly  
 250 at the outer bend. Furthermore, it shows uniform erosion at the inflow bedlevel, unlike *Sisyphé* (Figure 9), although  
 251 neither model predicts the inflow bedlevel particularly accurately.

252 For rigour, we run *Sisyphé* with these optimised values for viscosity and longitudinal slope. The resulting bedlevel  
 253 change is shown in Figures 12a and 12b at the 90° and 180° cross-sections, respectively. There is a slight improvement  
 254 in the values of the total relative error norm (46), which falls from 1.144 for the results from Villaret et al. (2013) to  
 255 1.067 for the optimised values. However, the errors of *Sisyphé* are still higher than those obtained for *Thetis*.

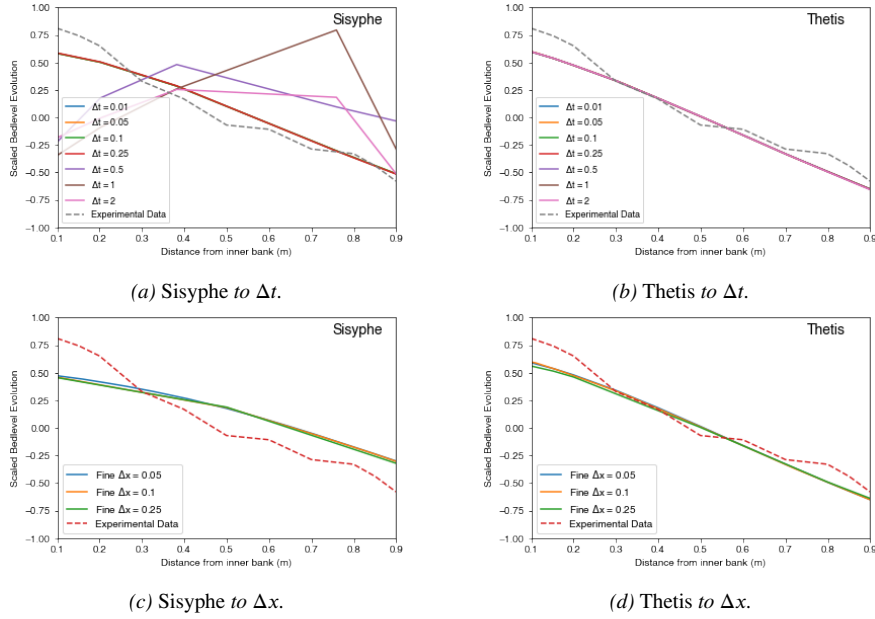


**Figure 13:** Sensitivity of bedlevel to  $\Delta x$  and  $\Delta t$  ( $90^\circ$  cross-section).

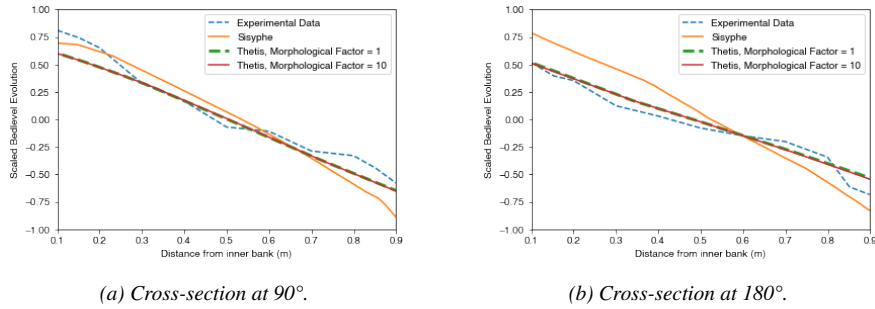


**Figure 14:** Scaled bedlevel evolution from *Thetis* ( $v = 0.05 \text{ m}^2 \text{ s}^{-1}$  and slope = 0.0035) with a morphological scale factor of 1 and 10, *Sisyph* Villaret et al. (2013) and experimental data Yen and Lee (1995).

#### 256 5.2.4. Sensitivity Study

257 Given *Sisyph*'s sensitivity to  $\Delta t$  discussed in Section 4.2.1, we conduct a sensitivity study on  $\Delta t$  and the mesh  
 258 step size,  $\Delta x$ , maintaining the ratio between the fine and coarse meshes at 2:5. We run *Sisyph* and use our optimised  
 259 viscosity and longitudinal slope values for consistency with *Thetis*.

260 Figure 13b shows *Thetis* is insensitive to  $\Delta t$ , whereas *Sisyph* in Figure 13a is sensitive to  $\Delta t$ , as in the migrating  
 261 trench test case. Although for  $\Delta t \leq 0.25 \text{ s}$  *Sisyph*'s results are robust, for larger  $\Delta t$  values they are both sensitive and  
 262 inaccurate. Furthermore, for this test case, *Thetis* converges for  $\Delta t < 10 \text{ s}$ , meaning it is much less computationally  
 263 expensive than *Sisyph*, which requires  $\Delta t \leq 0.25 \text{ s}$ .

264 Figures 13c and 13d show both models are relatively insensitive to the mesh step size  $\Delta x$ . There are slight differ-  
 265 ences when a fine  $\Delta x = 0.25 \text{ m}$  is used in both models, suggesting our choice of a fine  $\Delta x = 0.1 \text{ m}$  is appropriate.

266 As in Section 4.2, we assess whether *Sisyph* results depend on the discretisation of the advection terms. Our  
 267 preliminary results show that *Sisyph*'s sensitivity to  $\Delta t$  is independent of the choice of morphodynamic scheme,  
 268 as indicated in the previous example. The strict Courant number stability criteria of other *Sisyph* hydrodynamic  
 269 discretisations means they require small  $\Delta t$  to run and thus the effect is less noticeable.

270 Finally, Figures 14a and 14b provide an overview of our results and show not only that we have validated our  
 271 model, but that it is more accurate than *Sisyph* for this more complex test case. Figures 14a and 14b also confirm that  
 272 a morphological scale factor of 10 is appropriate because there is no observable difference between our results with a  
 273 morphological scale factor of 10 and 1 (*i.e.* no scaling).



**Table 4**

Comparison of computational time (seconds). For the migrating trench,  $\Delta t = 0.05$  s and increased  $\Delta t = 0.3$  s; for the meander  $\Delta t = 0.1$  s and increased  $\Delta t = 10$  s.

	<i>Sisyphé</i>	<i>Thetis</i>	<i>Thetis</i> (scale factor)	<i>Thetis</i> (scale factor, increased $\Delta t$ )
Migrating Trench	3,427	341,717	39,955	12,422
Meander	980	60,784	10,811	1,212

## 6. Benchmarking

Finally, we compare the computational times of *Thetis* and *Sisyphé* for both the test cases discussed in this work and summarise the results in Table 4. Note that for *Sisyphé* we have chosen the most efficient matrix storage method following guidance in Lang et al. (2014). When the same  $\Delta t$  and morphological scale factor are used in both models, *Thetis* is slower, partly since on the same mesh a DG discretisation possesses significantly more degrees of freedom. However, the robustness we get from *Thetis*'s DG based discretisation allows us to obtain accurate results with larger  $\Delta t$  values and the use of a morphological scale factor. If we take advantage of this, for the simple migrating trench test case, *Thetis* can be made competitive with *Sisyphé* and for the more complex meander test case the computational time is very similar. In Table 4, we use a moderate morphological scale factor of 10, but if we use a morphological scale factor of 50, for the meander test case *Thetis* takes less than half the time that *Sisyphé* does, with only very slight observable differences compared to with a morphological scale factor of 1. This is likely because for the simple test case, we have the disadvantages of the additional computational cost of DG without experiencing the advantages in robustness that DG exhibits for more complex cases.

## 7. Conclusion

In this work, we have presented a new 2D depth-averaged coupled hydrodynamic and sediment transport functionality within the finite element based coastal ocean model *Thetis*. Our model makes significant, novel contributions to the complex problem of modelling sediment transport. It is shown to be both accurate and stable, as well as comparable in computational cost to other standard models. To the best of our knowledge, it is the first full morphodynamic model employing a DG based discretisation. We report on several new capabilities within *Thetis*, including bedload transport, bedlevel changes, slope effect corrections, a secondary current correction, a sediment transport source term, a velocity correction factor in the sediment concentration equation, and a morphological scale factor. All these were validated using the migrating trench and meander test cases, indicating the significance of each of the additional components. The coupled and nonlinear nature of the problem makes this type of model very sensitive to parameter changes. However, *Thetis* is found to be largely insensitive to changes in timestep and mesh grid size, unlike the current state-of-the-art model *Sisyphé*, which is found to have a much larger variability, particularly with respect to the timestep in the case of the test cases considered in this work. In future work, we will use our model in a coastal zone case study requiring coupled wave and current modelling, and will further consider adjoint-based model calibration and the use of mesh adaptivity.

## Acknowledgements

The authors thank Dr Catherine Villaret for her help in the set-up of *Sisyphé*. MCAC's work was funded through the EPSRC CDT in Mathematics for Planet Earth. AA acknowledges the support of NERC through the fellowship grant NE/R013209/2. MDP, JRP and CJC acknowledge the support of EPSRC through the grants EP/R029423/1 and EP/R007470/1.

## Computer code availability

The relevant *Thetis* code for the morphodynamic model presented in this work can be found at [https://github.com/mc4117/morphodynamic\\_model](https://github.com/mc4117/morphodynamic_model).

## 310 References

- 311 Amoudry, L.O., 2008. A review on coastal sediment transport modelling. Proudman Oceanographic Laboratory, Liverpool, UK.
- 312 Amoudry, L.O., Souza, A.J., 2011. Deterministic coastal morphological and sediment transport modeling: A review and discussion. *Reviews of*  
313 *Geophysics* 49.
- 314 CIESIN, 2013. Low Elevation Coastal Zone (LECZ) Urban-Rural Population and Land Area Estimates, Version 2. NASA Socioeconomic Data  
315 and Applications Center (SEDAC), Palisades, New York, USA. URL: <https://doi.org/10.7927/H4MW2F2J>.
- 316 Danilov, S., 2013. Ocean modeling on unstructured meshes. *Ocean Modelling* 69, 195–210.
- 317 Dawson, C., Sun, S., Wheeler, M.F., 2004. Compatible algorithms for coupled flow and transport. *Computer Methods in Applied Mechanics and*  
318 *Engineering* 193, 2565–2580.
- 319 Deltares, 2014. Delft3D-FLOW Simulation of multi-dimensional hydrodynamic flows and transport phenomena including sediments. User Manual.  
320 Delft, The Netherlands. URL: [https://oss.deltares.nl/documents/183920/185723/Delft3D-FLOW\\_User\\_Manual.pdf](https://oss.deltares.nl/documents/183920/185723/Delft3D-FLOW_User_Manual.pdf).
- 321 Englund, F., 1974. Flow and bed topography in channel beds. *Journal of the Hydraulics Division* 100.
- 322 Epshteyn, Y., Rivière, B., 2007. Estimation of penalty parameters for symmetric interior penalty Galerkin methods. *Journal of Computational and*  
323 *Applied Mathematics* 206, 843–872.
- 324 Farrell, P.E., Ham, D.A., Funke, S.W., Rognes, M.E., 2013. Automated derivation of the adjoint of high-level transient finite element programs.  
325 *SIAM Journal on Scientific Computing* 35, C369–C393.
- 326 Garcia, M., Parker, G., 1991. Entrainment of bed sediment into suspension. *Journal of Hydraulic Engineering* 117, 414–435.
- 327 Gerritsen, H., de Goede, E., Platzek, F., van Kester, J., Genseberger, M., Uittenbogaard, R., 2008. Validation Document Delft3D-FLOW; a software  
328 system for 3D flow simulations. Technical Report. Deltares, Delft, The Netherlands.
- 329 Hervouet, J.M., 1999. TELEMAC, a hydroinformatic system. *Houille Blanche-revue Internationale De L Eau* 54, 21–28. doi:10.1051/1hb/  
330 1999029.
- 331 Hervouet, J.M., 2007. *Hydrodynamics of Free Surface Flows, Modelling with the Finite-element Method*. John Wiley & Sons Ltd, West Sussex,  
332 UK.
- 333 Huybrechts, N., Villaret, C., Hervouet, J.M., 2010. Comparison between 2D and 3D modelling of sediment transport: Application to the dune  
334 evolution, in: *Proceedings of the 5th International Conference on fluvial Hydraulics*, Braunschweig, Germany.
- 335 Kärnä, T., Kramer, S., Mitchell, L., Ham, D., Piggott, M., Baptista, A., 2018. Thetis coastal ocean model: discontinuous Galerkin discretization for  
336 the three-dimensional hydrostatic equations. *Geoscientific Model Development* 11, 4359–4382.
- 337 Kubatko, E.J., Westerink, J.J., Dawson, C., 2006. An unstructured grid morphodynamic model with a discontinuous Galerkin method for bed  
338 evolution. *Ocean modelling* 15, 71–89.
- 339 Kulkarni, V., Sahoo, N., 2013. Module 5: Viscous Incompressible flow; Lecture 5 : Internal Flow – Part IV. [https://nptel.ac.in/courses/  
340 101103004/module5/lec5/4.html](https://nptel.ac.in/courses/101103004/module5/lec5/4.html).
- 341 Landsberg, A., Chtchelkanova, A., Lind, C., Boris, J., Young, T., 1998. *Fast3D user and programmer reference manual*. US Naval Research  
342 Laboratory, Washington DC, USA.
- 343 Lang, P., Desombre, J., ATA, R., Goeury, C., Hervouet, J.M., 2014. TELEMAC-2D modelling system - User manual.
- 344 Leveque, R.J., 1996. High-resolution conservative algorithms for advection in incompressible. *SIAM Journal on Numerical Analysis* 33, 627–665.
- 345 Li, B.Q., 2006. *Discontinuous Finite Elements in Fluid Dynamics and Heat Transfer*. Springer Science & Business Media, Berlin, Germany.
- 346 McManus, T., Percival, J., Yeager, B., Barral, N., Gorman, G., Piggott, M., 2017. Moving mesh methods in Fluidity and Firedrake. Technical  
347 Report July. doi:10.13140/RG.2.2.27670.24648.
- 348 Michoski, C., Dawson, C., Mirabito, C., Kubatko, E.J., Wirasaet, D., Westerink, J.J., 2013. Fully coupled methods for multiphase morphody-  
349 namics. *Advances in Water Resources* 59, 95–110. URL: [http://dx.doi.org/10.1016/j.  
350 advwatres.2013.05.002](http://dx.doi.org/10.1016/j.advwatres.2013.05.002).
- 351 Pan, W., Kramer, S.C., Piggott, M.D., 2019. Multi-layer non-hydrostatic free surface modelling using the discontinuous Galerkin method. *Ocean*  
352 *Modelling* 134, 68–83.
- 353 Papanicolaou, A.T.N., Elhakeem, M., Krallis, G., Prakash, S., Edinger, J., 2008. Sediment transport modeling review - current and future develop-  
354 ments. *Journal of Hydraulic Engineering* 134, 1–14.
- 355 Park, S.W., Ahn, J., 2019. Experimental and numerical investigations of primary flow patterns and mixing in laboratory meandering channel. *Smart*  
356 *Water* 4, 4. URL: <https://doi.org/10.1186/s40713-019-0016-y>, doi:10.1186/s40713-019-0016-y.
- 357 Rathgeber, F., Ham, D.A., Mitchell, L., Lange, M., Luporini, F., McRae, A.T., Bercea, G., Markall, G., Kelly, P.H., 2017. Firedrake: automating  
358 the finite element method by composing abstractions. *ACM Transactions on Mathematical Software (TOMS)* 43, 24.
- 359 Roelvink, D., Van Dongeren, A., McCall, R., Hoonhout, B., Van Rooijen, A., Van Geer, P., De Vet, L., Nederhoff, K., Quataert, E., 2015. XBeach  
360 Technical Reference: Kingsday Release. Delft, The Netherlands: Deltares, Technical report .
- 361 Segur, H., 2009. Lecture 8 : The Shallow-Water Equations. Woods Hole Oceanographic Institution, Woods Hole, Massachusetts, USA.
- 362 Soulsby, R., 1997. *Dynamics of marine sands, a manual for practical applications*. Thomas Telford, London, UK.
- 363 Syvitski, J., Slingerland, R., Burgess, P., Meiburg, E., Murray, A.B., Wiberg, P., Tucker, G., Voinov, A., 2010. *Morphodynamic Models: An*  
364 *Overview*. River, Coastal and Estuarine Morphodynamics, RCEM 2009 , 3–20.
- 365 Talmon, A., Struiksma, N., Mierlo, M.V., 1995. Laboratory measurements of the direction of sediment transport on transverse alluvial-bed slopes.  
366 *Journal of Hydraulic Research* 33, 495–517.
- 367 Tassi, P., Rhebergen, S., Vionnet, C., Bokhove, O., 2008. A discontinuous Galerkin finite element model for river bed evolution under shallow  
368 flows. *Computer Methods in Applied Mechanics and Engineering* 197, 2930–2947.
- 369 Tassi, P., Villaret, C., 2014. *Sisyphé v6.3 User's Manual*. EDF R&D, Chatou, France.
- 370 Van Rijn, L.C., 1980. Storm surge barrier Oosterschelde-computation of siltation in dredged trenches: Semi-empirical model for the flow in dredged  
371 trenches. Deltares, Delft, The Netherlands.
- 372 Van Rijn, L.C., 1984. Sediment Transport, Part II: Suspended Load Transport. *Journal of Hydraulic Engineering* 110, 1613–1641.

- 373 Villaret, C., Hervouet, J.M., Kopmann, R., Merkel, U., Davies, A.G., 2013. Morphodynamic modeling using the Telemac finite-element system.  
374 Computers & Geosciences 53, 105–113.
- 375 Villaret, C., Kopmann, R., Wyncoll, D., Riehme, J., Merkel, U., Naumann, U., 2016. First-order uncertainty analysis using Algorithmic Differenti-  
376 ation of morphodynamic models. Computers & geosciences 90, 144–151.
- 377 Vouriot, C.V.M., Angeloudis, A., Kramer, S.C., Piggott, M.D., 2019. Fate of large-scale vortices in idealized tidal lagoons. Environmental Fluid  
378 Mechanics 19, 329–348.
- 379 Warner, J.C., Sherwood, C.R., Signell, R.P., Harris, C.K., Arango, H.G., 2008. Development of a three-dimensional, regional, coupled wave,  
380 current, and sediment-transport model. Computers & Geosciences 34, 1284–1306.
- 381 Warren, I., Bach, H., 1992. MIKE 21: a modelling system for estuaries, coastal waters and seas. Environmental Software 7, 229–240.
- 382 Wu, W., 2007. Computational river dynamics. CRC Press, Boca Raton, Florida, USA.
- 383 Yen, C.I., Lee, K.T., 1995. Bed topography and sediment sorting in channel bend with unsteady flow. Journal of Hydraulic Engineering 121,  
384 591–599.